



## Post-Processing in the Material-Point Method

Andersen, Søren; Andersen, Lars Vabbersgaard

*Publication date:*  
2012

*Document Version*  
Publisher's PDF, also known as Version of record

[Link to publication from Aalborg University](#)

*Citation for published version (APA):*  
Andersen, S., & Andersen, L. V. (2012). *Post-Processing in the Material-Point Method*. Department of Civil Engineering, Aalborg University. DCE Technical Memorandum No. 30

### General rights

Copyright and moral rights for the publications made accessible in the public portal are retained by the authors and/or other copyright owners and it is a condition of accessing publications that users recognise and abide by the legal requirements associated with these rights.

- Users may download and print one copy of any publication from the public portal for the purpose of private study or research.
- You may not further distribute the material or use it for any profit-making activity or commercial gain
- You may freely distribute the URL identifying the publication in the public portal -

### Take down policy

If you believe that this document breaches copyright please contact us at [vbn@aub.aau.dk](mailto:vbn@aub.aau.dk) providing details, and we will remove access to the work immediately and investigate your claim.

# **Post-Processing in the Material-Point Method**

**Søren Mikkelsen Andersen  
Lars Vabbersgaard Andersen**



**DEPARTMENT OF CIVIL ENGINEERING**  
AALBORG UNIVERSITY



Aalborg University  
Department of Civil Engineering  
Division for Structures, Materials and Geotechnics

**DCE Technical Memorandum No. 30**

# **Post-Processing in the Material-Point Method**

by

Søren Mikkelsen Andersen  
Lars Vabbersgaard Andersen

December 2012

© Aalborg University

## **Scientific Publications at the Department of Civil Engineering**

**Technical Reports** are published for timely dissemination of research results and scientific work carried out at the Department of Civil Engineering (DCE) at Aalborg University. This medium allows publication of more detailed explanations and results than typically allowed in scientific journals.

**Technical Memoranda** are produced to enable the preliminary dissemination of scientific work by the personnel of the DCE where such release is deemed to be appropriate. Documents of this kind may be incomplete or temporary versions of papers—or part of continuing work. This should be kept in mind when references are given to publications of this kind.

**Contract Reports** are produced to report scientific work carried out under contract. Publications of this kind contain confidential matter and are reserved for the sponsors and the DCE. Therefore, Contract Reports are generally not available for public circulation.

**Lecture Notes** contain material produced by the lecturers at the DCE for educational purposes. This may be scientific notes, lecture books, example problems or manuals for laboratory work, or computer programs developed at the DCE.

**Theses** are monographs or collections of papers published to report the scientific work carried out at the DCE to obtain a degree as either PhD or Doctor of Technology. The thesis is publicly available after the defence of the degree.

**Latest News** is published to enable rapid communication of information about scientific work carried out at the DCE. This includes the status of research projects, developments in the laboratories, information about collaborative work and recent research results.

Published 2012 by  
Aalborg University  
Department of Civil Engineering  
Sohngaardsholmsvej 57,  
DK-9000 Aalborg, Denmark

Printed in Aalborg at Aalborg University

ISSN 1901-7278  
DCE Technical Memorandum No. 30

**ISSN 1901-7278**  
**DCE Technical Memorandum No. 30**

# Post-Processing in the Material-Point Method

Søren Andersen\* and Lars Andersen

Department of Civil Engineering  
Aalborg University, Aalborg, Denmark  
e-mail: sa@civil.aau.dk

**Abstract** The material-point method (MPM) is a numerical method for dynamic or static analysis of solids using a discretization in time and space. The method has shown to be successful in modelling physical problems involving large deformations, which are difficult to model with traditional numerical tools such as the finite element method. In the material-point method, a set of material points is utilized to track the problem in time and space, while a computational background grid is utilized to obtain spatial derivatives relevant to the physical problem. Currently, the research within the material-point method focusses on establishing its accuracy and robustness. For easy evaluation of results, a good visualization of the deformation pattern as well as an accurate way to obtain the stresses are essential. This article introduces new ideas to improve the postprocessing of results obtained by the material-point method. The first idea involves associating a volume with each material point and displaying the deformation of this volume. In the discretization process, the physical domain is divided into a number of smaller volumes each represented by a simple shape; here quadrilaterals are chosen for the presented two-dimensional problems. At the centroid of each of these sub domains, a material point is defined. The deformation gradient tensor associated with the material point is used to display deformation of the sub domain. This type of visualization is shown to dramatically improve visualization of large strain problems. It is noted, that this idea is also relevant for other point based methods, such as smoothed particle hydrodynamics, where the history dependent variables are tracked by a set of particles. The second idea introduced in the article involves the fact that while the stresses may oscillate in an unphysical fashion at the individual material points, a physically realistic stress field may often be obtained at the grid nodes. Further, a new way of remapping the stresses via the grid nodes is introduced to obtain more meaningful stress fields in the postprocessing. The new ideas are shown to improve the visual presentation of results from material-point method simulations and hence the understanding of the underlying physical problems to which the method is applied. Further, the way the stresses can be extracted reveals some pitfalls for the method and suggests a place to direct future research.

**Keywords:** Material-point method; Numerical analysis; large deformations; point-based methods

## 1 Introduction

When evaluating results obtained by a numerical simulation for continuum in dynamical problems, three types of visualizations are of interest: 1. Movements and deformations, 2. velocities, 3. stresses and strains.

For the material-point method(MPM), it is straightforward to visualize movement of relatively rigid bodies. This can be done most simple by displaying the position of the individual material points using small dots. Visualization of this type is presented amongst others by Sulsky and co-workers (1; 2; 3) and by Cummins and Brackbill (4). By only displaying positions of the points, no direct visualization of deformation is obtained. The challenge arises when the deformations become significant.

For problems involving large deformations, it is useful to compare finite-element-based methods to particle-based methods which assign material properties to a set of points or particles, such as the material-point method. In general, the finite element software is at a much more advanced

stage than the software for particle based methods. A treatment of various ways to postprocess results from a finite element solution is found in the work of Babuška and Miller (5; 6; 7). In finite element methods, a direct visualization of the deformation of the material is obtained as the finite element mesh directly tracks the deformation, and finite element software typically displays the deformation using the position of the nodes along with an isoparametric tracking of the element boundaries. At the same time, the distortion of the finite element mesh is known to degenerate the accuracy of the solution. A way to maintain accuracy of the finite element mesh is to perform remeshing during a simulation. This remeshing replaces the distorted elements with new, undistorted elements. Hence, the very direct way of visualizing local deformations by displaying the distorted mesh becomes impossible. Another issue is how to perform remeshing and mapping of material properties for complex material models.

The advantage of the particle-based methods is that no mesh distortion occurs, as the state variables is not directly associated with a mesh, but associated with a set of particles or material points. Technically, the material-point method can be thought of as an Arbitrary Lagrangian Eulerian formulation, where the mesh is reset at each time step.

For the material-point method, a challenge is how to display the deformation, as only the coordinates of each material point directly enter the algorithm. Similarly, with only a coordinate its not immediately obvious how to visualize other field quantities such as stresses. A simple way to visualize field quantities involves associating a volume with each material point, with the material point located at the centroid of each volume. This volume can then be translated around according to the position of the material point as obtained by the numerical solution. By having a finite sized volume associated with each material point it is for instance possible to assign a colour to each volume, where the colour represents a physical quantity. An example is a colour scale for a particular component of the stress tensor when a colour plot shows the variation of that stress component. It could also show the velocity components or other data of interest, or it could even be useful to just assign different colours to the material points to easier see the deformation pattern. This type of visualization is among others utilized by Andersen and Andersen (8) to visualize evolution of landslides.

In this article, it is demonstrated that it is easy to extend this type of visualization to directly show the deformations. This is obtained by introducing the deformation gradient tensor as a state variable for the material points. The technique of tracking the deformation tensor is firstly introduced by Guilkey and Weiss (9). The application of the deformation gradient tensor to display the deformations seems to have been developed independently both by Andersen (10) and by Choudhury et al. (11). A material point is assigned an initial configuration. Here, each material points is discretized as an initially rectangular quadrilateral to model two-dimensional problems. The deformation of each material point is visualized by calculating the deformed configuration of the quadrilateral using the deformation gradient tensor. This type of visualization is shown to give a much better visualization of the deformations.

For the purpose of displaying the velocities, two types of visualizations are of interest; vector plots and colour plots. A vector plot is made by associating a length scale with the velocity, the velocity components associated with the material point then defines the length and direction of the vector. The vector plot has the advantage that it is possible to visualize all components in the velocity vector. The colour plot on the other hand needs to either chose one of the velocity components or the speed of the particle as it can only plot scalar fields can be plotted in this manner. In general,

vector plots are good at visualizing the direction of the velocity or other first order tensors while the colour plots makes it easier to see the magnitude of individual components.

Another issue that requires attention is the stresses and the strains. Here, its useful to note the difference of the material-point method to a finite element formulation. In the finite element formulation both the stresses and the strains are obtained in the post-processing, most often obtained by interpolation and extrapolation of quantities obtained at Gauss points. In the material-point method on the other hand, the stresses are tracked at the material points themselves. It has been reported by several sources that the stresses are often seen to be inaccurate when displayed directly using the material points. This is reported by Shin (12) and by Andersen and Andersen (13) among others. Especially, for problems involving large deformations the stresses show wild oscillations. The stress oscillation is often so extreme that it is a surprise that the general physics (for instance the deformation pattern) is accurately described. In the initial articles on the MPM (1; 2), it was reported that the method was meshless in the sense that all history dependent variables are only carried by the material points. However, as shown here, this may not be so simple. Thus, it is possible to extract the physically realistic stresses from very unrealistic and oscillatory stress fields at the material points by mapping to the grid nodes and back to the material points in the postprocessing. This is very useful for illustration purposes, but it also suggest that the way the method handles stresses should be closer examined in subsequent work.

On the other hand, the strains are not part of the material-point method computational scheme, only the strain increments associated with a particular time step are. Therefore, the total strains may be extracted in the post-processing. In the formulation presented here, where the deformation-gradient tensor is tracked for each material point, the most natural way to extract the strains is to calculate them from the deformation gradient tensor. For linear elastic materials, another way is to calculate them from the stresses using the flexibility tensor. The two ways of extracting the strains will generally yield different results.

Firstly, the MPM-calculation scheme is presented in Section 2. A review of material point visualizations along with a suggestion of a new way of visualizing the deformation is presented in Section 3.

The latter part of the article discusses and illustrate various postprocessing tools which are illustrated using two example problems. Section 4 defines the two example problems. Section 5 discusses ways to visualize movements and deformations, while Section 6 discusses ways to visualize the velocities. Section 7 discusses how the strain field and the stress field can be visualized and reports a remarkable feature of the stress field, namely that realistic stresses are only found using postprocessing via the grid nodes. Further, discussions of stress invariants as well as elasto-plastic stress and strain measures are included. Finally, Section 8 presents the conclusions.

## 2 The computational scheme in the material-point method

### 2.1 Governing equations

The governing equation of the material-point method is the balance of momentum, given by

$$\rho \frac{d\mathbf{v}}{dt} = \nabla \cdot \boldsymbol{\sigma} + \rho \mathbf{b}, \quad (1)$$



where  $\rho = \rho(\mathbf{x}, t)$  is the current density,  $\mathbf{v} = \mathbf{v}(\mathbf{x}, t)$  is the spatial velocity,  $\boldsymbol{\sigma} = \boldsymbol{\sigma}(\mathbf{x}, t)$  is the Cauchy stress tensor and  $\mathbf{b} = \mathbf{b}(\mathbf{x}, t)$  is the specific body force. The spatial coordinate is denoted  $\mathbf{x}$  and  $t$  is the time.

Equation (1) is cast in weak form by multiplication by an arbitrary test function,  $\mathbf{w}$ , and integration over the domain,  $\Omega$ , yielding

$$\int_{\Omega} \rho \mathbf{w} \cdot \frac{d\mathbf{v}}{dt} dV = \int_{\Omega} \mathbf{w} \cdot \nabla \cdot \boldsymbol{\sigma} dV + \int_{\Omega} \rho \mathbf{w} \cdot \mathbf{b} dV. \quad (2)$$

Using Green's divergence theorem, Eq. (2) can be reformulated as

$$\int_{\Omega} \rho \mathbf{w} \cdot \frac{d\mathbf{v}}{dt} dV = - \int_{\Omega} \boldsymbol{\sigma} : \nabla \mathbf{w} dV + \int_{\partial\Omega_{\tau}} \mathbf{w} \cdot \boldsymbol{\tau} dS + \int_{\Omega} \rho \mathbf{w} \cdot \mathbf{b} dV, \quad (3)$$

where  $\boldsymbol{\tau}$  is the surface traction vector and  $\partial\Omega_{\tau}$  is the part of the boundary with known traction. Next, the framework of the generalized interpolation material-point method (14) is utilized to discretize Eq. (3).

The domain is represented by a finite set of material volumes. The initial domain  $\Omega^0$  is divided into a set of non-overlapping subdomains  $\Omega_p^0$ , where  $p = 1, 2, \dots, N_p$  and  $N_p$  is the number of material volumes. At the centroid of each subdomain, a material point with the coordinates  $\mathbf{x}_p$  is defined. For clarity,  $\Omega_p^0$  denotes the initial domain while the volume of this domain is denoted  $V_p^0$ . Hence, given an initial density field  $\rho^0(\mathbf{x})$ , the initial volume and the mass associated with material point  $p$  is given by

$$V_p^0 = \int_{\Omega_p^0} dV \quad (4)$$

and

$$m_p = \int_{\Omega_p^0} \rho^0(\mathbf{x}) dV, \quad (5)$$

respectively, whereas

$$\rho_p^0 = \frac{m_p}{V_p^0} \quad (6)$$

is introduced as the density of material point  $p$  in the initial configuration.

The velocity and stress associated with a material point are defined as volume-weighted quantities, i.e.

$$\mathbf{v}_p = \frac{1}{V_p^0} \int_{\Omega_p^0} \mathbf{v}^0(\mathbf{x}) dV \quad (7)$$

and

$$\boldsymbol{\sigma}_p = \frac{1}{V_p^0} \int_{\Omega_p^0} \boldsymbol{\sigma}^0(\mathbf{x}) dV. \quad (8)$$

Similarly, external body forces are defined by

$$\mathbf{b}_p = \frac{1}{V_p^0} \int_{\Omega_p^0} \mathbf{b}(\mathbf{x}) dV. \quad (9)$$

Although associated with the material volumes, the quantities defined by Eqs. (4) to (9) will, in accordance with existing MPM articles, be referred to as material-point quantities.

In order to obtain a discrete spatial representation, particle characteristic functions,  $\chi_p$ , associated with the material points are defined. The particle characteristic functions are defined such that they are a partition of unity in the reference configuration, i.e.

$$\sum_{p=1}^{N_p} \chi_p^0(\mathbf{x}) = 1 \quad \forall \mathbf{x} \in \Omega_0. \quad (10)$$

Further, the particle characteristic functions are normalized with respect to the initial volume, i.e.

$$\int_{\Omega^0} \chi_p(\mathbf{x}, t) dV = V_p^0. \quad (11)$$

In this article, constant particle characteristic functions are employed defined by

$$\chi_p^0(\mathbf{x}) = \begin{cases} 1 & \text{if } \mathbf{x} \in \Omega_p, \\ 0 & \text{otherwise} \end{cases} \quad (12)$$

Further, it is noted that the original MPM formulation (1) is obtained by setting  $\chi_p = \delta(\mathbf{x} - \mathbf{x}_p)$ , where  $\delta$  is the Dirac delta function.

The material point quantities defined in Eqs. (5) to (9) are used to approximate the fields for the momentum, the body forces and stresses in the balance of momentum, respectively. Field quantities are represented as sums over the material points, i.e.

$$f(\mathbf{x}) = \sum_{p=1}^{N_p} f_p \chi_p(\mathbf{x}). \quad (13)$$

For instance, the first term in the balance of momentum is represented by

$$\rho \frac{d\mathbf{v}}{dt} \cong \sum_{p=1}^{N_p} \rho_p \frac{d\mathbf{v}_p}{dt} \chi_p(\mathbf{x}) = \sum_{p=1}^{N_p} \frac{m_p}{V_p} \frac{d\mathbf{v}_p}{dt} \chi_p(\mathbf{x}). \quad (14)$$

Using the material-points representation in the balance of momentum yields

$$\begin{aligned} \sum_{p=1}^{N_p} \frac{m_p}{V_p} \int_{\Omega_p} \mathbf{w} \cdot \frac{d\mathbf{v}_p}{dt} \chi_p dV &= \int_{\partial\Omega_\tau} \mathbf{w} \cdot \boldsymbol{\tau} dS - \sum_{p=1}^{N_p} \boldsymbol{\sigma}_p : \int_{\Omega_p} \frac{\partial \mathbf{w}}{\partial \mathbf{x}} \chi_p dV \\ &+ \sum_{p=1}^{N_p} \frac{m_p \mathbf{b}_p}{V_p} \int_{\Omega_p} \mathbf{w} \chi_p dV, \end{aligned} \quad (15)$$

where  $V_p$  is the current volume of the material point.

In the implementation employed here, the current volume will be calculated using the determinant of the deformation gradient tensor associated with the material point. Section 3 shows how the deformation gradient tensor is calculated for each material point. The term on the left hand side of Eqs. (15) represents the rate of change of momentum. On the right hand side the first term represents the surface tractions, the second term represents internal forces due to stress gradients

while the last term represents external body forces. Further, it is noted that the physical quantities are evaluated at each material point.

Now, approximations for the field of test functions are made in terms of the background grid. The geometry of the grid is defined by  $N_n$  nodes, using the index  $i = 1, \dots, N_n$  exclusively to identify the nodes. Between the nodes, the test functions are represented continuously by means of nodal shape functions by

$$\mathbf{w}(\mathbf{x}) \cong \sum_{i=1}^{N_n} \mathbf{w}_i N_i(\mathbf{x}), \quad (16)$$

while the gradients of the test function are represented by

$$\frac{\partial \mathbf{w}(\mathbf{x})}{\partial \mathbf{x}} \cong \sum_{i=1}^{N_n} \mathbf{w}_i \frac{\partial N_i(\mathbf{x})}{\partial \mathbf{x}}. \quad (17)$$

As for the particle characteristic function, the nodal shape functions are required to be a partition of unity, i.e.

$$\sum_{i=1}^{N_n} N_i(\mathbf{x}) = 1 \quad \forall \mathbf{x}, \mathbf{x} \in \Omega_c, \quad (18)$$

where  $\Omega_c$  is the computational domain.

Employing Eqs. (16) and (17), the balance of momentum can be written as

$$\begin{aligned} \sum_{i=1}^{N_n} \mathbf{w}_i \cdot \left( \sum_{p=1}^{N_p} m_p d \frac{\mathbf{v}_p}{dt} \frac{1}{V_p} \int_{\Omega_p \cap \Omega_i} N_i \chi_p dV \right) &= \sum_{i=1}^{N_n} \mathbf{w}_i \cdot \left( \int_{\partial \Omega_\tau \cap \Omega_i} N_i \boldsymbol{\tau} dS \right) \\ - \sum_{i=1}^{N_n} \mathbf{w}_i \cdot \left( \sum_{p=1}^{N_p} \int_{\Omega_p \cap \Omega_i} \boldsymbol{\sigma}_p \cdot \frac{\partial N_i}{\partial \mathbf{x}} \chi_p dV \right) &+ \sum_{i=1}^{N_n} \mathbf{w}_i \cdot \left( \sum_{p=1}^{N_p} m_p \mathbf{b}_p \frac{1}{V_p} \int_{\Omega_p \cap \Omega_i} N_i \chi_p dV \right), \end{aligned} \quad (19)$$

where  $\Omega_i$  is the domain where  $N_i$  is nonzero.

Now, the weighting and the gradient weighting function are introduced as

$$\bar{N}_{ip} = \frac{1}{V_p} \int_{\Omega_p \cap \Omega_i} N_i \chi_p dV \quad (20)$$

and

$$\frac{\partial \bar{N}_{ip}}{\partial \mathbf{x}} = \frac{1}{V_p} \int_{\Omega_p \cap \Omega_i} \frac{\partial N_i}{\partial \mathbf{x}} \chi_p dV. \quad (21)$$

Utilizing that the test functions  $\mathbf{w}_i$  are arbitrary, the system of equations need to be satisfied at all grid nodes. Employing Eqs. (20) and (21) in Eq. (19) yields

$$\sum_{p=1}^{N_p} m_p \frac{d\mathbf{v}_p}{dt} \bar{N}_{ip} = \int_{\partial \Omega_\tau^0} N_i \boldsymbol{\tau} dS - \sum_{p=1}^{N_p} \boldsymbol{\sigma}_p V_p \frac{\partial \bar{N}_{ip}}{\partial \mathbf{x}} + \sum_{p=1}^{N_p} m_p \mathbf{b}_p \bar{N}_{ip}. \quad (22)$$

Rewriting the balance of momentum yields

$$m_i \frac{d\mathbf{v}_i}{dt} = \mathbf{f}_i^{int} + \mathbf{f}_i^{ext}, \quad (23)$$

where

$$m_i \frac{d\mathbf{v}_i}{dt} = \sum_{p=1}^{N_p} m_p \frac{d\mathbf{v}_p}{dt} \bar{N}_{ip} \quad (24)$$

is the nodal momentum rate of change,

$$\mathbf{f}_i^{int} = - \sum_{p=1}^{N_p} \sigma_p V_p \frac{\partial \bar{N}_{ip}}{\partial \mathbf{x}} \quad (25)$$

is the internal force and

$$\mathbf{f}_i^{ext} = \int_{\partial\Omega_\tau} N_i \boldsymbol{\tau} dS + \sum_{p=1}^{N_p} m_p \mathbf{b}_p \bar{N}_{ip} \quad (26)$$

is the external force. The GIMP formulation leads to a system of equations almost identical to the MPM equations, only in the GIMP formulation the governing equation is assembled using the weighting function  $\bar{N}_{ip}(\mathbf{x}_p, t)$  instead of  $N_i(\mathbf{x}_p, t)$  which is used in the MPM.

The question for the GIMP based implementations is how to obtain the integrals of Eq. (20) and Eq. (21). As noted by Bardengagen and Kober (14), if the evaluation of these integrals were to take the deformation of the material point domains into account, it would not be possible to obtain them analytically. In this implementation, approximate evaluation of Eq. (20) and Eq. (21) are obtained as proposed by Ma et al. (15) by performing a bi-linear integration over a rectangular domain associated with the material point. Hence, the particle characteristic function is assembled as

$$\chi_p = \chi_p^x(x) \chi_p^y(y), \quad (27)$$

where  $x, y$  are the two components of the material point position,  $\mathbf{x}$ . In the initial configuration, the size of an equivalent rectangle, which is used to form the GIMP functions, is determined by the discretization and denoted  $\mathbf{l}_p^0 = (l_p^{0,x}, l_p^{0,y})^T$ . At a later time, the lengths used to determine the GIMP integrals are given by

$$l_p^x = l_p^{0,x} (\det(\mathbf{F}_p))^{1/2} \quad \text{and} \quad l_p^y = l_p^{0,y} (\det(\mathbf{F}_p))^{1/2}, \quad (28)$$

where  $\mathbf{F}_p$  is the deformation gradient tensor associated with the material point. Section 3 presents an algorithm for obtaining and tracking the deformation gradient tensor at the material points. Using a bi-linear particle characteristic function has the advantage that the weighting functions can be obtained as bi-linear products of the one-dimensional weighting function for which an analytical solution is presented by Bardenhagen and Kober (14). Employing Eqs.(27,28) is computationally very fast. Alternatively, as described by Bardenhagen and Kober (14) and as shown by Andersen (10), numerical integration of the weighting and the gradient weighting function can be performed.

## 2.2 Explicit time-integration approach

The basic idea is to solve the balance of momentum on the grid and then use the information to update the quantities associated with the material points. The mass and momentum at grid node  $i$  are found by

$$m_i^k = \sum_{p=1}^{N_p} m_p \bar{N}_{ip} \quad (29)$$

and

$$m_i^k \mathbf{v}_i^k = \sum_{p=1}^{N_p} \mathbf{v}_p^k m_p \bar{N}_{ip}, \quad (30)$$

respectively. The index  $k$  denotes the  $k$ th. time step.

The position and the velocity updates for the material points are given by

$$\mathbf{x}_p^{k+1} = \mathbf{x}_p^k + \Delta t \sum_{i=1}^{N_n} \bar{N}_{ip} \frac{m_i^k \mathbf{v}_i^k + \frac{1}{2} \Delta t (\mathbf{f}_i^{int,k} + \mathbf{f}_i^{ext,k})}{m_i^k} \quad (31)$$

and

$$\mathbf{v}_p^{k+1} = \mathbf{v}_p^k + \Delta t \sum_{i=1}^{N_n} \bar{N}_{ip} \frac{(\mathbf{f}_i^{int,k} + \mathbf{f}_i^{ext,k})}{m_i^k}. \quad (32)$$

A simple MPM/GIMP algorithm using explicit time-integration can be given as:

1. Initialisation of material properties at the material points at time  $t = 0$  ( $k = 0$ ).
2. At each time step:
  - A background computational grid is generated (in this implementation, the same grid is generated/reset at each time step),
  - the shape/weighting and the gradient shape/weighting functions are determined,
  - masses and velocities at the grid nodes is found,
  - stresses and strain increments are determined,
  - internal and external forces are calculated,
  - the position and the velocity of the material points are found,
  - other relevant variables associated with the material points are updated,
  - time is incremented.

### 3 Classical material point visualizations and suggested improvement using the deformation gradient tensor

Most of the articles which apply the material-point method display the material points simply as points, i.e. small dots. Time dependent problems are illustrated by letting the points move through space over time.

A logical extension of the visualization can be obtained by tracking deformation of the volumes associated with the individual material points. The geometric volume (three-dimensional model) or area (two-dimensional model) associated with a material point is given the notion “voxel”. In the reference configuration, the voxel is defined such that  $V_p^0$  corresponds to the size of the voxel. The voxel notion is introduced by Steffen et al. (16). The deformation of each voxel can be tracked by introducing a deformation-gradient tensor, which needs to be tracked through the simulation. Obtaining the deformation gradient tensor is easy, since grid velocities are calculated at each time step as part of the method.

For this type of visualization to be useful, a voxel shape suited to displaying deformation needs to be chosen. For instance, a circle-shaped voxel is not appropriate for displaying shear deformations. However, a discretization, where the domain is divided into rectangular voxels is useful, and this type of discretization is easy to implement. In order to display the deformed state, the location of corners of a voxel is calculated using the deformation gradient.

A simple way to implement the tracking is presented. A deformation gradient is initially associated with each material point in the initial configuration.

$$\mathbf{F}_p^0 = \frac{\partial \mathbf{x}_p}{\partial \mathbf{x}_0} = \frac{1}{V_p} \int_{\partial \Omega_p^0} \mathbf{F}(\mathbf{x}) dV \quad (33)$$

In the initial configuration, the deformation gradient tensor is prescribed. Typically, and undeformed material state will be prescribed, i.e.  $\mathbf{F}^0 = \mathbf{I}$ , where  $\mathbf{I}$  is the identity tensor. An explicit forward difference updating scheme is employed to update the deformation gradient tensor,

$$\mathbf{F}^{k+1} = \Delta \mathbf{F}^{k+1} \mathbf{F}^k, \quad (34)$$

where  $\mathbf{F}^{k+1}$  is the deformation gradient at timestep  $k + 1$ ,  $\mathbf{F}^k$  is the deformation gradient at timestep  $k$  and  $\Delta \mathbf{F}^{k+1}$  is the deformation taking place between the time steps. Expressing the time derivative of the deformation gradient as  $\partial \mathbf{F} / \partial t = \partial \mathbf{v} / \partial \mathbf{x}^0$ ,  $\Delta \mathbf{F}^{k+1}$  can be expressed as

$$\Delta \mathbf{F}^{k+1} = \mathbf{I} + \Delta t \frac{\partial \mathbf{v}^k}{\partial \mathbf{x}^0}. \quad (35)$$

Using the nodal shape functions, the change in deformation gradient at an arbitrary point  $\mathbf{y}$  can be evaluated as

$$\Delta \mathbf{F}^{k+1}(\mathbf{y}) = \mathbf{I} + \Delta t \sum_{i=1}^{N_n} \mathbf{v}_i^k \left. \frac{\partial N_i^k(\mathbf{x})}{\partial \mathbf{x}} \right|_{\mathbf{x}=\mathbf{y}}. \quad (36)$$

For the material point, the increment of the deformation gradient is then calculated as

$$\Delta \mathbf{F}_p^{k+1} = \mathbf{I} + \Delta t \sum_{i=1}^{N_n} \mathbf{v}_i^k \frac{\partial N_{ip}}{\partial \mathbf{x}}. \quad (37)$$

This way of integrating the deformation gradient, using the grid velocities, is also employed by Guilkey and Weiss (9) and Love and Sulsky (17).

Employing the deformation gradient to track the deformation of the voxel associated with the material point presumes that there is a uniform deformation within the voxel. This concept is illustrated in Figure 1.

The tracking of the deformation gradient tensor can be applied to provide a better visualization of problems involving large strains. Considering a voxel associated with a material point, initially located at  $\mathbf{x}_p$ , the coordinate for a corner in the initial configuration can be written as

$$\mathbf{x}_C^0 = \mathbf{x}_p^0 + d\mathbf{x}^0, \quad (38)$$

where  $\mathbf{x}_C^0$  is the location of the corner and  $d\mathbf{x}^0$  is the line segment between the material point and the corner. At an arbitrary time, the location of the corner is given as

$$\mathbf{x}_C = \mathbf{x}_p + d\mathbf{x}. \quad (39)$$

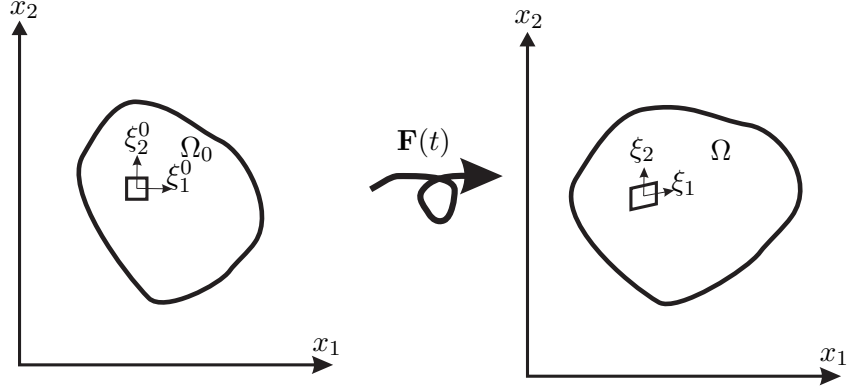


Fig. 1. Tracking the voxel associated with a material point through the deformation gradient tensor,  $\mathbf{F}$ . The local coordinates  $(\xi_1, \xi_2)^T$  determine the deformation of the voxel.

Using the deformation gradient, defined at the material point, the line segment can be calculated by

$$d\mathbf{x} = \mathbf{F} d\mathbf{x}^0, \quad (40)$$

where  $d\mathbf{x}^0$  is the deformed line segment and  $\mathbf{F}$  is the deformation-gradient tensor defined in the local coordinate system  $(\xi_1, \xi_2)^T$  by

$$\mathbf{F}^{local} = \frac{\partial \boldsymbol{\xi}}{\partial \boldsymbol{\xi}^0}. \quad (41)$$

Using the chain rule, the deformation gradient tensor in the global coordinate system becomes

$$\mathbf{F} = \frac{\partial \mathbf{x}}{\partial \boldsymbol{\xi}} \frac{\partial \boldsymbol{\xi}}{\partial \boldsymbol{\xi}^0} \frac{\partial \boldsymbol{\xi}^0}{\partial \mathbf{x}^0}, \quad (42)$$

where the coordinate-systems are defined on Figure 1.

In the examples presented later, the initial local axes are chosen along the global coordinate system. Hence, in this case

$$\frac{\partial \mathbf{x}}{\partial \boldsymbol{\xi}} = \mathbf{I} \quad \text{and} \quad \frac{\partial \mathbf{x}^0}{\partial \boldsymbol{\xi}^0} = \mathbf{I} \quad (43)$$

When the local voxel coordinates are coincident with the global coordinate system, the deformation gradient tensor reduces to

$$\mathbf{F} = \frac{\partial \boldsymbol{\xi}}{\partial \boldsymbol{\xi}^0}. \quad (44)$$

#### 4 Definition of example problems

In order to examine the different techniques of visualization, it is advantageous to have a few simple examples. Virtually any example involving a material subjected to large deformations may be appropriate. Two simple problems are chosen.

Firstly, the example of colliding discs, initially presented by Sulsky et al. (1), is revisited. The configuration of the problem is shown in Figure 2.

In the work by Sulsky, the example is employed to show that MPM is able to model dynamic problems in an easy way. The contact between the discs is handled automatically by the MPM

Material properties for both discs:

$$\rho_0 = 20, \quad E = 10^5, \quad \nu = 0.3$$

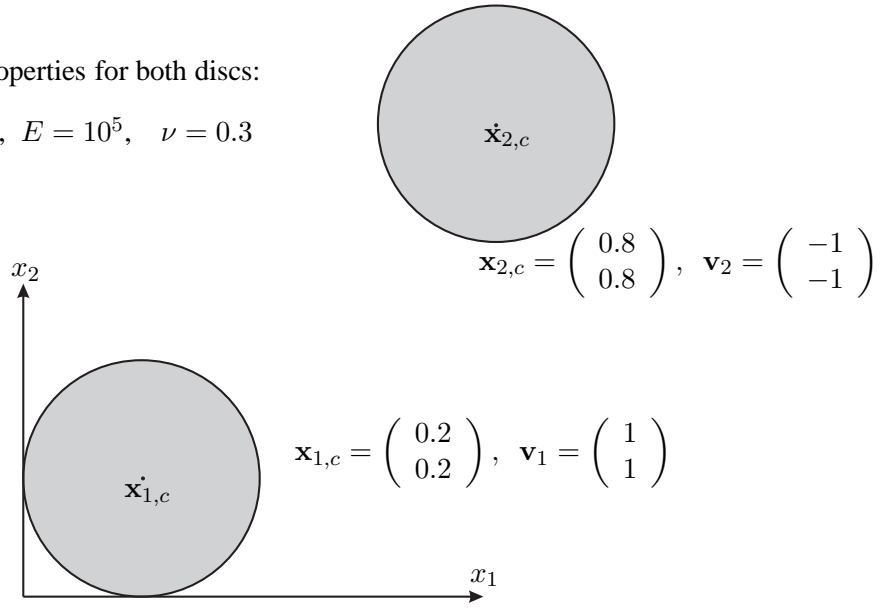


Fig. 2. The colliding discs problem

algorithm presented above. Some of the material points from the two discs will eventually interpolate to the same grid nodes. When the two discs interpolate to the same grid nodes, the two discs share the same velocity field and strain gradients will develop during the collision. This results in a stress wave in each disc which eventually will cause bounce off when an elastic material model used for the discs. However, as shown later, this way of automatically handling contact does not extend well to other types of colliding bodies. For instance, two blocks colliding would tend to stick to each other. Hence, York et al. (18) suggested to model colliding bodies using a separate set of grid nodes for each body, and to handle the interaction using a contact law where no tension stresses are allowed to take place upon the end of impact. These ideas have later been extended by Bardenhagen and co-workers (19; 20) to handle frictional contact between colliding bodies. For this example, the intrinsic MPM contact approach by means of a shared velocity field, also called “no-slip” contact works fine. In some analysis of large deformations presented the following, the example is modified slightly by modelling the two discs as Tresca materials with cohesion  $c = 5$ .

A second example, the collapse of a soil column, is introduced in order to study the effects of the proposed large-strain formulation as well as to study stress distributions obtained by the MPM. Figure 3 shows the initial configuration of the collapsing soil column. A rectangular block of soil is placed on a frictional surface.

The experiment, typically performed by kids in a sandbox, of filling a bucket with fine grained, dry sand and placing the bucket carefully with the open side on flat ground and quickly lifting the bucket is similar to which should happen, only in the soil column example, plane strain is assumed. The soil column will collapse, as it is not supported on its sides.

The soil is modeled as a frictional material by employing the Mohr-Coulomb material model. In the Mohr-Coulomb model a yield function,  $f$ , is defined. The yield function determines the response based on a yield criterion, where  $f < 0$  implies elastic response, while  $f = 0$  leads to elasto-plastic response. The Mohr-Coulomb yield function is defined in terms of principle stresses



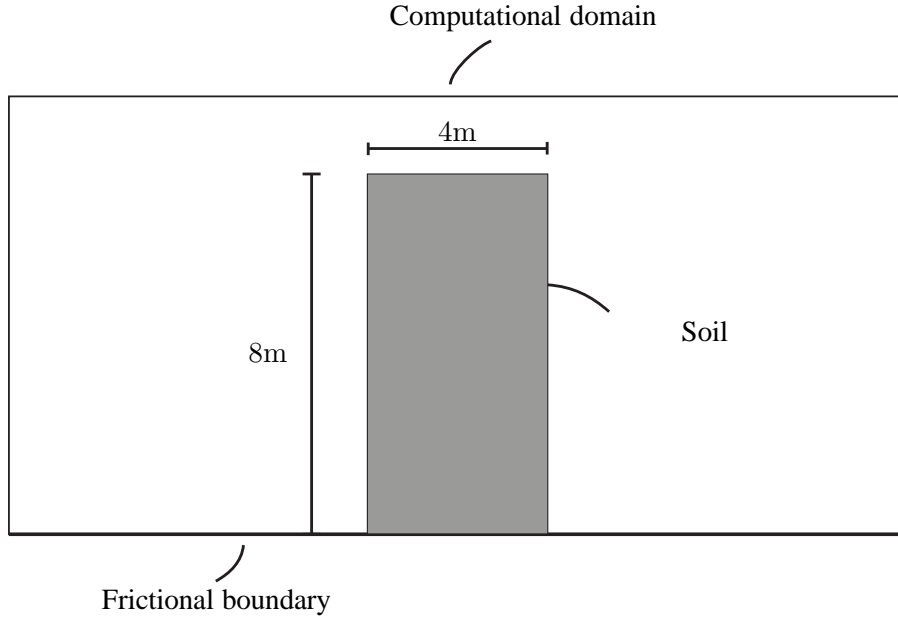


Fig. 3. The collapsing soil column problem.

by

$$f = \frac{1}{2}(\sigma_3 - \sigma_1) + \frac{1}{2}(\sigma_1 + \sigma_3) \sin \varphi - c \cos \varphi, \quad (45)$$

where  $\varphi$  is the angle of friction and  $c$  is the cohesion. The principal stresses are considered positive in tension and  $\sigma_1 \leq \sigma_2 \leq \sigma_3$ . The second principal stress is assumed not to influence the strength provided by the Mohr-Coulomb criterion.

The stress rate is given in terms of the elastic strain increment, i.e.

$$\dot{\boldsymbol{\sigma}} = \mathbf{C} : (\dot{\boldsymbol{\epsilon}} - \dot{\boldsymbol{\epsilon}}^p), \quad (46)$$

where  $\dot{\boldsymbol{\epsilon}}$  is the total strain rate,  $\dot{\boldsymbol{\epsilon}}^p$  is the plastic rate and  $\mathbf{C}$  is the elastic constitutive tensor. The plastic strain increment is found using the relation

$$\dot{\boldsymbol{\epsilon}}^p = \dot{\lambda} \frac{\partial g}{\partial \boldsymbol{\sigma}}, \quad (47)$$

where  $\dot{\lambda}$  a positive scaling factor and  $g$  is the plastic potential function given by

$$g = \frac{1}{2}(\sigma_3 - \sigma_1) + \frac{1}{2}(\sigma_1 + \sigma_3) \sin \psi. \quad (48)$$

Here  $\psi$  is the angle of dilatation of the soil. In the numerical solution, finite stress increments are considered. The stress increment is calculated by firstly calculating an elastic predictor stress. This elastic predictor stress may be outside the yield surface. An efficient return of the stresses back to the yield surface is obtained by the algorithm proposed by Clausen et al. (21).

The soil is described using the following set of material properties:

$$E = 20\text{MPa}, \quad \nu = 0.25, \quad \rho_0 = 10^3\text{kg/m}^3, \quad c = 1\text{kPa}, \quad \phi = 40^\circ \quad \text{and} \quad \psi = 0^\circ. \quad (49)$$

A frictional coefficient  $\mu = 0.6$  is prescribed at the lower boundary.

An initial  $K_0$ -stress state is specified with the vertical normal stress given by

$$\sigma_{yy}^0 = -dg\rho^0, \quad (50)$$

where  $g = 9.8\text{m/s}^2$  is the acceleration of gravity and  $d$  is the distance from the top soil surface. The initial horizontal normal stresses are given by

$$\sigma_{xx}^0 = \sigma_{zz}^0 = -dg\rho^0 K_0, \quad (51)$$

where the earth pressure coefficient is given by  $K_0 = 1 - \sin \varphi$ . It is noted that this definition of  $K_0$  is not consistent with the chosen Poisson ratio, which suggest a lower  $K_0$ . The reason is that the soil behaves one way when depositing, during which the lateral earth pressures are developed and in another way when subjected to loading, in this case the stress relieve and subsequent collapse. The chosen Poisson ratio represents a realistic ratio for the elastic behaviour of a dense sand. Finally,  $\sigma_{xy}^0 = 0$  is prescribed for all material points. At the bottom of the modelled domain, a frictional boundary condition is specified, given in terms of a coefficient of friction  $\mu$ . Obviously, as the soil is not supported in the horizontal direction, the stresses cannot be sustained and a plastic collapse will occur.

A simple way of implementing a frictional boundary condition is suggested. The resulting force, as calculated from the right-hand side of Eq. (23), is decomposed into a normal component,  $f_n$ , and a tangential component,  $f_t$ . The normal force is considered positive if it is directed outward from the boundary. Friction is only present in the case of compressive normal force, i.e. when  $f_n > 0$ , and separation is allowed otherwise. In addition to the internal and external forces, a frictional force is introduced, given by

$$f_t \leq \mu f_n, \quad (52)$$

where  $\mu$  is the coefficient of friction. Two estimates of the velocity at the end of the time step are calculated: The velocity without any friction and the velocity with full friction. The velocity without any friction is solved from Eq. (23) as

$$\tilde{v}_t^{i,k+1} = v_t^{i,k} + \frac{\Delta t}{m_i} (f_t^{i,int} + f_t^{i,ext}) \quad (53)$$

and the estimated velocity in the case of full friction is given by

$$\hat{v}_t^{i,k+1} = v_t^{i,k} + \frac{\Delta t}{m_i} (f_t^{i,int} + f_t^{i,ext} + f_t^{i,fric}), \quad (54)$$

where the frictional force is given by  $f_t^{i,fric} = -\text{sign}(v_t^{i,k})\mu f_n$ . In the case of  $\tilde{v}_t^{i,k+1}\hat{v}_t^{i,k+1} > 0$ , full friction is present and the resulting force is given by the force term of Eq. (54). Otherwise, the friction stops the material and the resulting force present in the node is given by

$$f_t^{i,res} = -\frac{m_i v_t^{i,k}}{\Delta t}. \quad (55)$$

The algorithm presented is simpler than the algorithm presented by Wieckowski et al. (22) and avoids the need to specify any penalty parameters. However, it will be demonstrated in the following that useful results are obtained.

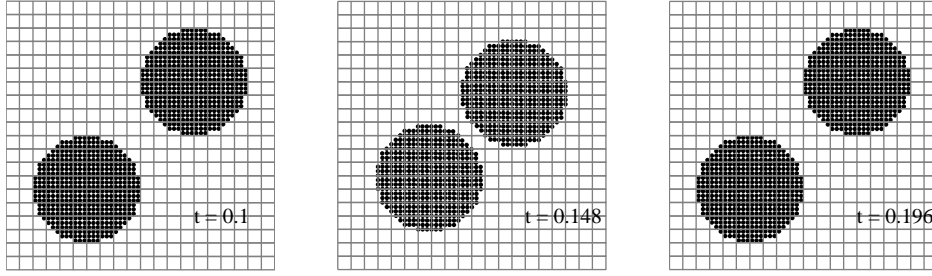


Fig. 4. Position of material points as a function of time. The discs collide and then bounce off.

## 5 Visualization of movements and deformations

Firstly, the classical MPM visualization, where the positions of the particles are displayed as points is shown. The position of the material points are shown as a function of time in Figure 4 for the colliding discs problem.

### 5.1 Using the deformation gradient tensor to track the deformation

Another type of visualization is to associate a rectangle with each material, where the size of the rectangle is given by the discretization and the material point is placed in the centre of it. The visualization is then to let the rectangle move through space over time. Using this, it is possible to display physical quantities by associating a colour scale with a selected material property. Visualization, where the initial size of the rectangle simply translates through time with the material point in the centre are presented by Andersen and Andersen (8). A better visualization can be obtained by letting the rectangle deform as given by the deformation gradient tensor. Figure 5 shows the final configuration of the collapse of the plastic discs with a voxels that are only translated governed by the position of the material points, and voxels that are updated using the deformation gradient tensor. As is seen from Figure 5, the use of the deformation gradient tensor significantly improves the visual appearance of the discs. The remainder of the figures of this article are all employing this visualization technique.

### 5.2 Using conceptual colouring schemes for easier visualization of deformation

In order to show how the discs deform, representative colouration may be employed. For instance, the discs may be striped or checkered for a better visualization. Stripes may run along the  $x$ -axis, the  $y$ -axis, or they have a rotation relative to the grid. In order to illustrate representation of deformation, the example is modified slightly. The two discs are now modeled as a Tresca material with a cohesion of  $c = 5$ . Figure 6 shows the initial and the final configuration of the discs using different ways to colour the material for visualization purposes. It is observed that when a plastic material-model is employed, the discs will stick to each other upon impact. Further, it is noted that adding a colouring scheme solely for visualization purposes is able to give a better visualization of the deformation than just using a uniform colour for each disc.

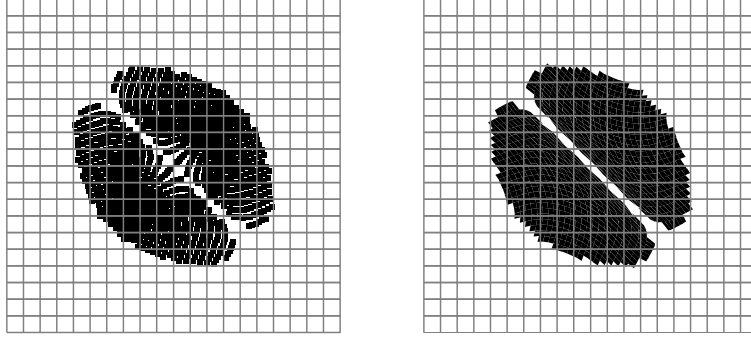


Fig. 5. Final configuration for the collapse of the plastic discs. Left: Voxels are defined by rectangles with size defined by the initial discretization and position governed by the material point. Right: The deformation gradient tensor is applied to find the deformed voxels.

### 5.3 Using colour scale plots to illustrate deformation pattern and field quantities

In bodies that are subject to large local deformations, it is often useful to visualize the magnitude of the movements and deformations. In order to show this, the example of the colliding soil column is explored. The dynamic simulation is performed with a time step of  $\Delta t = 0.001\text{s}$ . The simulation is performed until the soil has reached a state of vanishing velocities. For the present model the time of the collapse is  $t = 2.5\text{s}$ . The model consists of 4050 material points. Firstly, a colour plot of the deformation pattern for the collapse is shown in Figure 7. In the figure, another phenomena is observed, namely that the deformations degenerate some of the voxels near the bottom so much that they obtain string-like shapes. In relation to the collapse of the soil column, the displacement of the individual material points can be tracked using the simple relation

$$\mathbf{u}_p(t) = \mathbf{x}_p(t) - \mathbf{x}_p^0, \quad (56)$$

where  $\mathbf{x}_p^0$  is the initial position of the material point. Figure 8 shows the two components of the displacement vector as well as the magnitude of displacement. The soil column collapses around a relatively fixed core. A model with a lower coefficient of friction on the boundary may provide another picture. Especially, if the friction of the lower boundary is smaller than the internal friction of the soil, another pattern will appear where the soil would slide, or almost flow along the friction boundary.

### 5.4 Perspectives of the new way of visualizing the deformation

As shown in Figure 5, the tracking of the deformation gradient tensor is able to significantly improve the visualization of deformation. As applied, the tracking of the deformed voxels is applied solely as a postprocessing tool. In other words, the original MPM formulation is not altered. Hence, it can easily be incorporated in any MPM codes by tracking the deformation gradient tensor and calculating the deformed voxel configuration. The deformation gradient tensor is updated at each time-step. If output is only needed at some of the time steps, the deformed voxel configuration only needs to be calculated at these time-steps. Also, this type of visualization can without any

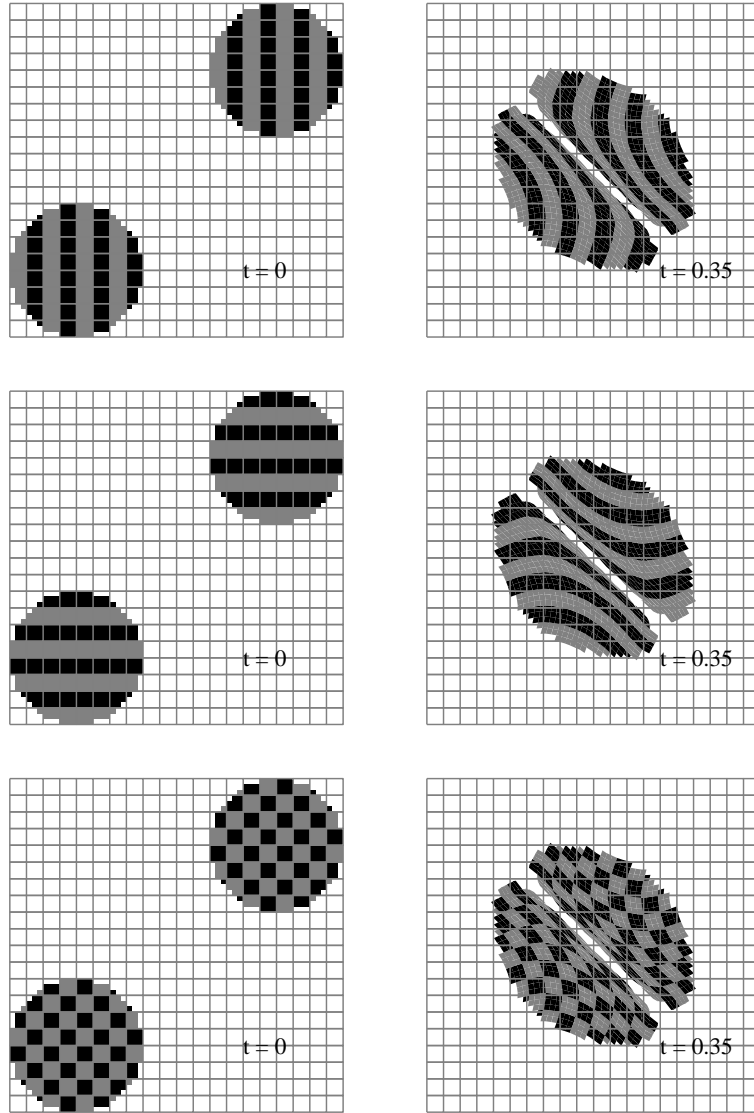


Fig. 6. Initial and final configuration of voxels of the two plastic discs using different colouring schemes for visualization purposes

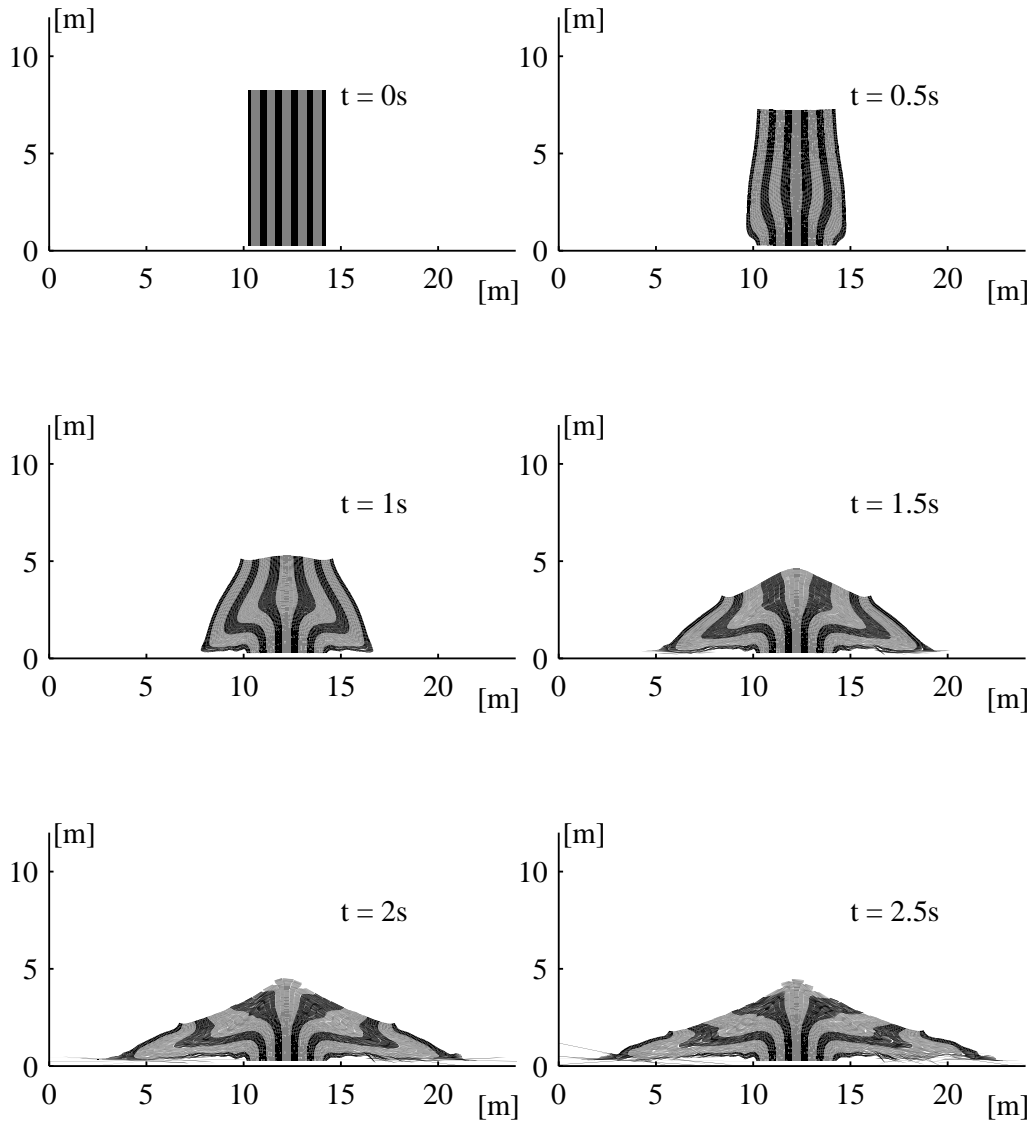


Fig. 7. Deformation pattern of the collapsing soil column.

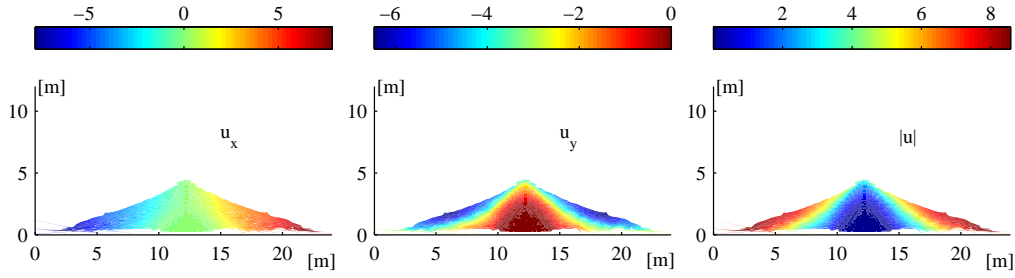


Fig. 8. Measures of displacement for the collapsing soil column.

problems be applied to other particle-based methods, such as smoothed particle hydrodynamics, where the typical visualizations also include plots of points, similar to Figure 4 (23; 24; 25). Visualizations, where the voxels are updated by the deformation gradient tensor, provides a very useful tool, as it makes it easy to see the deformation pattern. It is noted that visualization of deformations is automatically included in the finite-element method, as the deformation of nodes relatively to each other along with element boundaries provides a visualization similar to that of the figures which track the deformation of the voxels. The better description of the deformation obtained using this may also be able to suggest if there is anything wrong with the model, for instance if the discretization is too coarse to capture the deformation pattern — something which is harder, given only the position of material points. In the case of the collapsing soil column, some of the voxels got so distorted that they obtained string-like shapes, suggesting that a moderation would be beneficial here. For instance, those material points subjected to large shear deformation could be split into new ones. Further, the visualization verified that the overall deformation pattern looks realistic.

However, it should be explored in subsequent articles how to apply the knowledge obtained by this tracking to improve the MPM/GIMP models more directly, hence not only as a postprocessing tool. Possible ways to utilize the knowledge of the deformed configuration and the deformation gradient tensor include:

1. Apply the the knowledge of the deformed configuration of material points to dynamically update the discretization using splitting of material points into new ones, for instance where the largest strains are observed;
2. Provide a more accurate way to interpolate between the material-points and the mesh. The presented update scheme for the deformation gradient tensor and tracking deformed voxels provides knowledge of the deformed configuration of the material points, making evaluating of GIMP weighting functions over the deformed configuration possible.

## 6 Visualizing of velocities

The visualization of velocity is closely linked to the visualization of the deformation. For visualization of velocities, two types of plots are of interest – vector plots and colour plots. Vector plots

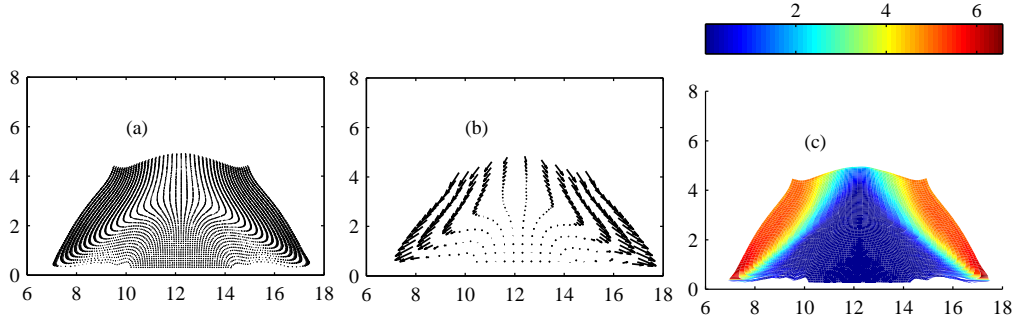


Fig. 9. Velocity and speed of the collapsing soil column, 1.15seconds into the collapse. (a) Vector plot of the velocities using all the material points. (b) Vector plot of the velocities using only a 1/16th of the material points – 1 of 4 in each direction. (c) The speed of the material points using a large strain representation and a color scale.

are useful to show in which direction the material is moving, but it may not be the most appropriate in order to visualize the magnitude of the deformation. Figure 9 shows the two ways of visualizing the velocity or the speed using both a vector plot and a colour plot. Further, it is demonstrated how the visual appearance of the vector plot can be improved by only including some of the material points. Clearly, it is hard to get a good view of a fine model if all the material points are included. Hence, for this simulation and simulations involving more material points, only some of the material points should be included in the visualization. It is also observed that the colour plot is much easier to get an idea of the magnitude of the speed.

## 7 Visualization of stresses and strains

Stresses and strains are both second order tensor fields which are generally harder to visualize directly than scalar and vector fields. It is possible to represent a stress tensor in two dimensions in a way similar to the vector plots of the velocity field. For two dimensional problems, there are three independent components of the stress tensor, but there exist an orientation of a cartesian coordinate system in which the shear stress vanishes and only two normal stresses exists. Orientation of this coordinate system is known as the principal directions and the normal stress components are the principal stresses. The principal stresses are also used to formulate the governing equations for the material model for the soil in the collapsing soil column as shown in Section 4. A plot of the principal stresses or the principal strains along with the corresponding directions can be performed by showing the principal stresses as crosses, where the length of the sides of the crosses are associated with stress scale and the orientation by the orientation of the crosses. This kind of plot is amongst many others utilized by the Finite Element Software Plaxis (26). An experienced user will also be able to give an idea of potential shear by comparing the magnitude of the principal stresses. The alternative is to use colour plots to display either component of the tensors or invariants associated with the tensors and will be employed in the following. The stresses and strains will be dealt with separately in the following subsections. Further, visualization of quantities of specific relevance



for elasto-plastic problems are dealt with in Subsection 7.4.

### 7.1 New method for visualization of the stresses

As shown by Andersen and Andersen (13) for the classical problem of a cantilevered beam, although the stresses at the individual material points may oscillate in a physically incorrect fashion, these physically unrealistic oscillations are not observed if the stresses are transferred to and displayed by the grid-nodes. This suggest that unlike the claims in the first MPM articles, it is not only the material points which carry information about the physics. If a spatially fixed mesh is employed, much of the interesting physics is tied to the grid nodes, where the equation of motion is resolved. This constitutes a theoretical problem for the material-point method, as it claims that the mesh is in essence unimportant as no state variables are associated with it.

Leaving this aside, it is demonstrated here how a simple mapping of the stresses from the material points to the grid nodes and back to the material points can extract the physical part of the stress in cases, where the stress field tracked by the individual material points is significantly degenerated.

Firstly, grid node stress tensors are defined by

$$\sigma_i = \sum_{p=1}^{N_p} \frac{\sigma_p \Phi_{ip} m_p}{m_i}, \quad (57)$$

where  $\sigma_i$  is the stress tensor, associated with grid node  $i$ ,  $\sigma_p$  is the stress tensor of material point  $p$ ,  $\Phi_{ip}$  is the interpolation function, in this implementation the GIMP weighting functions, while  $m_i$  and  $m_p$  are the nodal and material point masses, respectively. Using the nodal stresses, a smoothed material point stress tensor is defined as

$$\sigma_p^{smooth} = \sum_{i=1}^{N_n} \sigma_i \Phi_{ip}. \quad (58)$$

The extraction of a smoothed stress field is performed only as a postprocessing operation. Hence, it can be applied only to the time steps, where data is stored, which is typically only a small part of the total number of time steps in an explicit MPM/GIMP model. The result of this type of postprocessing is shown in the following example.

Figure 10 and 11 show the dynamical evolution of the vertical normal stress as obtained at the individual material points and calculated by Eq. (58), respectively. It is clearly seen that the visualization using mapping via the grid nodes provides a realistic evolution of the vertical normal stresses while the visualization based on the individual material-point stresses yields a very noisy stress field.

In the final configuration of the collapsed, it is possible to recognize the corners of the column from the initial configuration due to the presence of a small cohesion. It is clearly observed that the stress field at the individual points are very oscillatory to an extent, where it should not yield the correct behaviour, but a physically realistic result is nevertheless obtained. Also, it is observed that using the simple postprocessing of the stresses using the mapping via the grid nodes, a physically realistic variation of the vertical normal stress is obtained. As Eq. (58) is only applied as a postprocessing tool, the question arises as to why the deformation is captured so well, when the

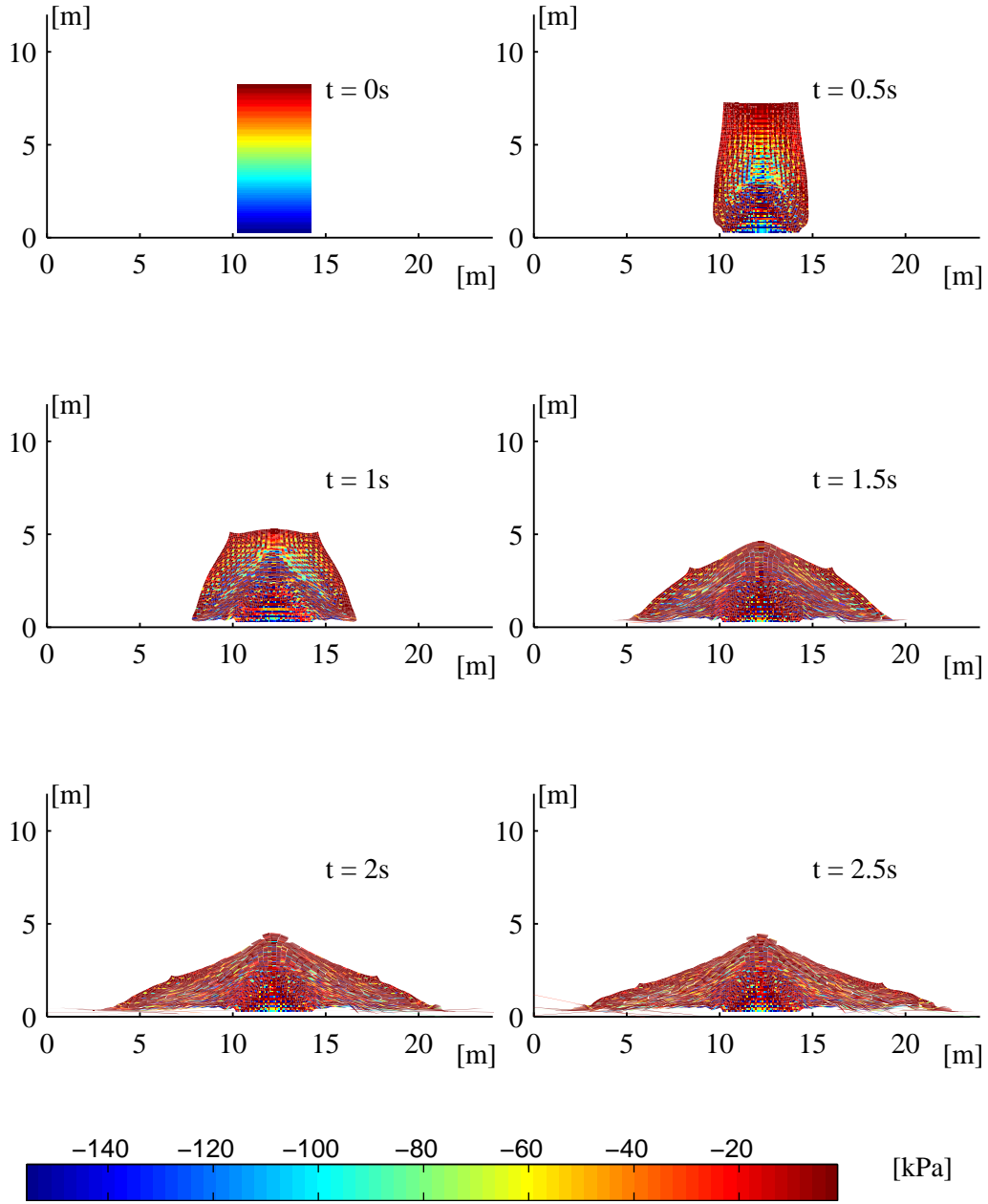


Fig. 10. Vertical normal stresses at the individual material points.

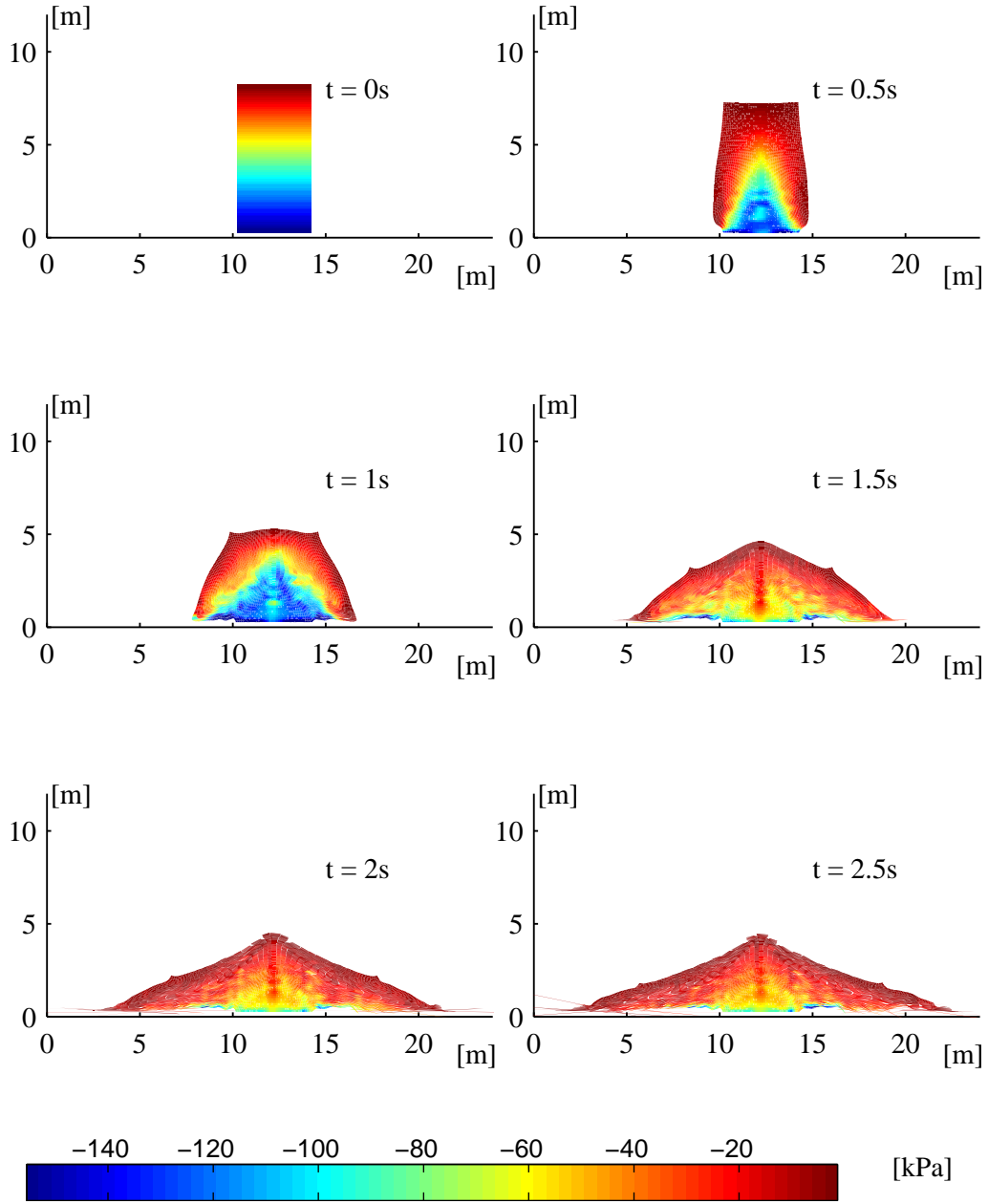


Fig. 11. Vertical normal stress visualization using Eq. (58).

stresses at the individual material points are unrealistic. Here, it must be observed that the collapsing soil column is a very homogeneous problem in both the stresses and the deformation pattern. Firstly, the deformation pattern is simple despite the large strains — it is basically a square transforming into a triangle. Secondly, the physical stress field is simple; initially, all the sides of the square will experience a stress relief governed by the plastic collapse, and the soil will eventually become stable, with the largest normal stresses under the middle, where the overburden pressure is largest. This suggest that for homogenous problems the method works well in capturing very large deformations and it is possible to extract a realistic stress field using an appropriate postprocessing. But the very inhomogeneous and inaccurate stresses at the individual material points is a large cause of concern in respect to problems, where a smoothing over element sizes may not be appropriate.

## 7.2 Visualization of stress invariants

As shown from Figure 11, the vertical normal stress component of the stress tensor has a much smoother and physically plausible spatial variation for the stress field calculated using Eq. (58). In addition to displaying stress components of the stress tensor, it is useful to display invariants of the stress tensor. For elasto-plastic problems such as the collapsing soil column, invariants of interest are

1. Principal stresses,  $\sigma_1, \sigma_2, \sigma_3$ , and the orientation of the principal stresses
2. The mean stress,  $p$
3. The deviatoric stress,  $q$

For the current implementation of two-dimensional plane strain model, the principal stresses are found by

$$\sigma_{1,3} = \frac{\sigma_{xx} + \sigma_{yy}}{2} \pm \sqrt{\left(\frac{\sigma_{xx} - \sigma_{yy}}{2}\right)^2 + \sigma_{xy}^2}, \quad (59)$$

where  $\sigma_{1,3}$  is the first and third principal stress (dependent on the sign in the equation), and  $\sigma_{xx}, \sigma_{yy}, \sigma_{xy}$  are the in-plane cartesian stresses. The intermediate principal stress is the out-of-plane stress, which is also tracked using the constitutive model. The angle,  $\theta$ , between the cartesian coordinate system used to describe the stress state and the principal stresses is given by

$$\tan 2\theta = \frac{\sigma_{xx} - \sigma_{yy}}{2\sigma_{xy}} \quad (60)$$

Additionally, the mean stress,  $p$ , and the deviatoric stress,  $q$ , are defined by

$$p = \frac{\sigma_{xx} + \sigma_{yy} + \sigma_{zz}}{3} \quad \text{and} \quad (61)$$

$$q = \sqrt{\frac{(\sigma_1 - \sigma_2)^2 + (\sigma_2 - \sigma_3)^2 + (\sigma_1 - \sigma_3)^2}{2}}. \quad (62)$$

Noting the differences between the stresses at the material points, and the stresses extracted using Eq. (58), there are different way ways of extracting invariants also:

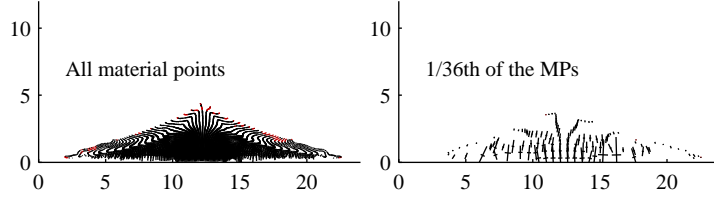


Fig. 12. Cross-plots of the principal stresses calculated using the smoothed stress field from Eq. (58). A black colour is utilized for compressive principal stresses and a red colour is employed for tensile principal stresses.

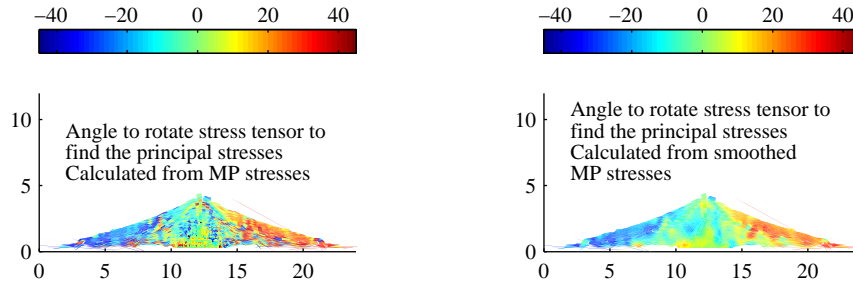


Fig. 13. Rotation (in degrees) of in-plane principal stresses compared to the horizontal and vertical axis, shown as a colour plot with and without the suggested smoothing method. The given solution is the shortest possible rotation, negative or positive, which is within 45 degrees.

1. Invariants associated with the material point stresses directly
2. Invariants calculated from the stresses found using Eq. (58)

The invariants could also be calculated using the material point stresses, and then be smoothed using an operation similar to the operation performed using Eqs. (57),(58). This will provide the same result as the second of the above methods.

First, visualization the of principal stresses is considered. A plot often used in finite element analysis of two-dimensional problems is to display the principal stresses as crosses which shows the orientation of the principle stresses and where the length of the lines that make the cross defines the magnitude according to to a user chosen stress length scale. Figure 12 shows the principal stresses calculated using a nodal smoothing. The figure uses a different amount of the material points to visualize the principle stress fields, to show that often, for such plots, its advantageous to only use some of the material points. In order to compare the principal stresses with and without nodal smoothing, the rotation of the principal stress axes compared to the  $x - y$ -axis,  $\theta$ , is shown using a colour plot in Figure 13. Next, the mean and the deviatoric stress tensors are shown for the two methods of extracting invariants in Figure 14. As seen, the smoothing process suggested also improves the description of the stress invariants.

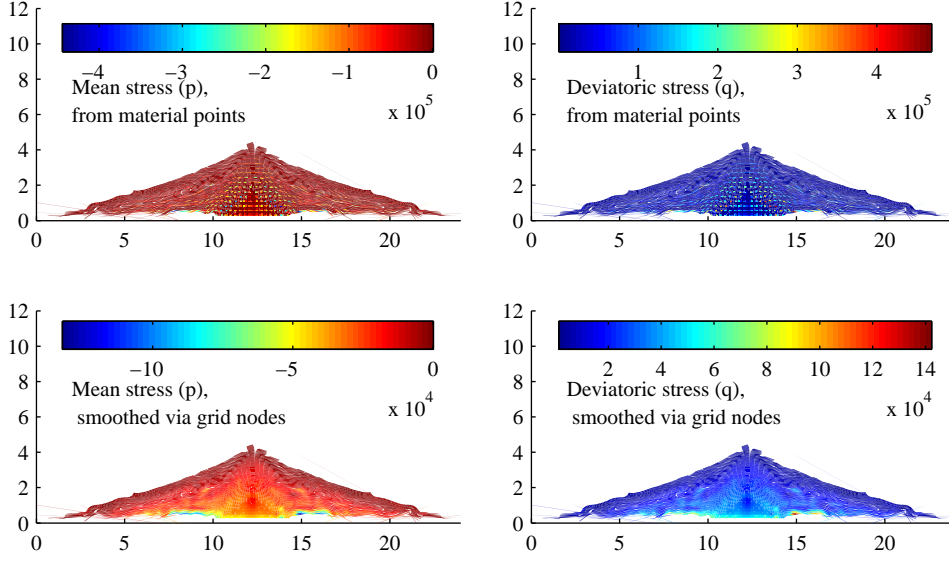


Fig. 14. Mean stress,  $p$ , and deviatoric stress,  $q$ , at the end of the soil-column collapse directly evaluated from the material point stresses and using a smoothing using the grid nodes.

### 7.3 Measures of total strain

In the material-point method computational scheme, the total strains do not enter the computational scheme. This leaves a freedom to how the strains are calculated and visualized. The total strain can be extracted from the MPM-computational scheme by either of the following methods

1. Integrating the strain increments over time in the MPM time integration;
2. Extraction using the deformation gradient tensor.

Direct integration of the strain increments is suggested by Sulsky et al. (2). Alternatively, the deformation gradient tensor is used to calculate the desired strain measure, such as the Green strain tensor or the engineering strain tensor or the logarithmic strain tensor. As the deformation gradient tensor is tracked as part of the current scheme for visualization of deformation, the latter is the natural choice here.

As the deformation patterns shown in Figure 7 and the left illustration in Figure 5 are physically realistically, all total strain measures extracted from the deformation gradient tensor will also be realistic. For small deformations, the so-called small-strain tensor or engineering strain tensor is most often used as strain measure.

Using the deformation gradient tensor, the engineering stress tensor can be calculated from

$$\epsilon_p = \frac{1}{2} (\mathbf{F}_p^T + \mathbf{F}_p) - \mathbf{I}. \quad (63)$$

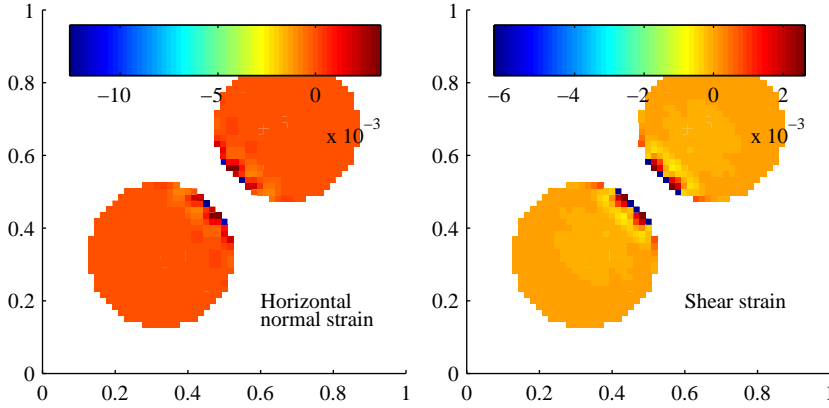


Fig. 15. Engineering strain components, extracted using the deformation gradient tensor, when the two discs are components, due to the symmetry of the problem, the vertical and the horizontal normal strain are the same for this problem.

The components of the engineering strain tensor, calculated using the deformation gradient tensor, are shown for the two discs in Figure 15. The engineering strain tensor in Eq. (63) can also potentially be employed for linear elastic problems to calculate stresses as an alternative to the material point stresses. It is observed, that in doing so, no visible differences has been observed between stresses calculated using the engineering strains from Eq. (63) and the stresses at the material points.

For larger deformations, the engineering strain tensor performs poorly and other strain measures are often employed. For moderately large strains, the Green strain tensor is defined by

$$\mathbf{E}_p = \frac{1}{2} (\mathbf{F}_p^T \mathbf{F}_p - \mathbf{I}) \quad (64)$$

For very large strains, the best strain measure is the logarithmic strain, or Hencky strain tensor, defined by

$$\mathbf{E}_p^{\ln} = \ln(\mathbf{U}_p), \quad (65)$$

where  $\mathbf{U}_p = (\mathbf{F}_p^T \mathbf{F}_p)^{\frac{1}{2}}$  is the right material stretch tensor associated with material point  $p$ , and  $\ln()$  denotes the natural logarithm of a second order tensor. The natural logarithm is here calculated using the explicit formula presented by Jog (27).

In order to compare the three different strain measures for a problem subjected to very large strains, the collapsed soil column is considered. Figure 16 shows a colour plot of the strain components of the three strain tensors, where a colour axis is defined from extreme values within each plot. It is observed that for extreme strains, as observed for some of the material points, the Green strain tensor components get very large values. On the contrary, the logarithmic strain tensor components vary smoothly and within a limited range. The development of strain through the collapse of the soil column in three material points are illustrated in Figure 17 for the horizontal normal component of the three different strain tensors and for a few selected material points. As seen from Figure 17, for small strains (Point C), the three strain measures are almost identical. For large strains, the Green strain tensor components become very large, while the logarithmic strain tensor components are smaller.

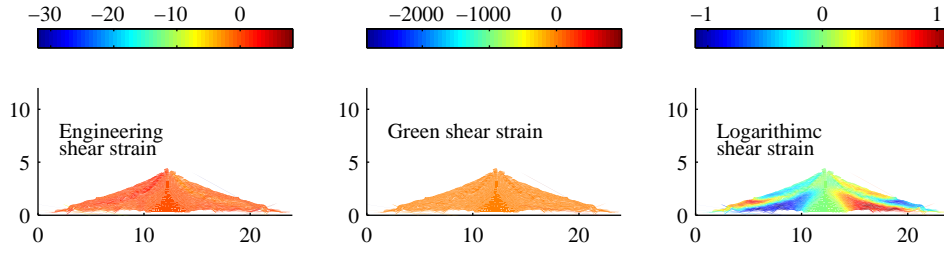


Fig. 16. Shear strain components of the engineering strain, the Green strain and the logarithmic strain tensors respectively. The strain tensors are extracted as part of postprocessing using the deformation gradient for each material point. The color scale above each plot is defined from extreme values from each plot. As seen, the logarithmic strain tensor is very good at capturing the deformation pattern while the two other colour scales are a degenerated by a few severely distorted material points.

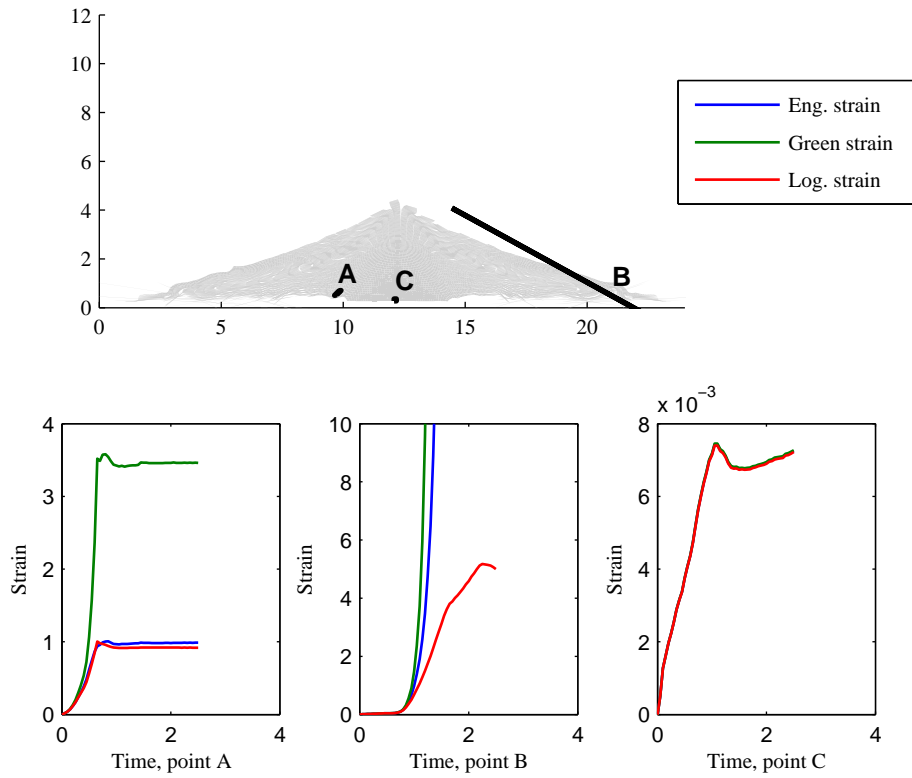


Fig. 17. Horizontal normal strain for the collapse of the soil column using the different strain measures. For small strain (point C), the three curves are almost coincident. For extreme strain (Point B) the logarithmic strain maintains a limited value while the engineering strain and the Green strain accelerates. For large strains (point A), the logarithmic strain and the engineering strain are very similar while the green strain component is larger.



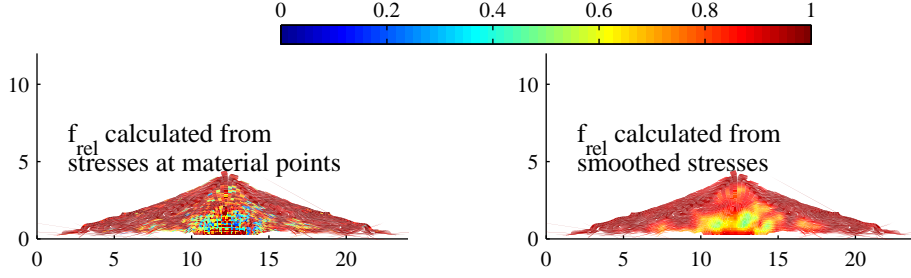


Fig. 18. Relative yield function (Eq. (66)) at the end of the collapse of the soil column, using the direct material point stresses and the stresses calculated using Eq. (58) respectively.

#### 7.4 Elasto-plastic stress and strain measures

An important class of problems to analyse and understand is elasto-plastic problems. The collapse of the soil column is a good example of a plastic collapse, and so is the collision of the two discs, when the discs are modelled as Tresca material.

In the collapse of the soil column, the elastic stresses cannot be sustained, and plastic strains will develop in the material. As observed from Figure 10, the direct material-point stresses exhibit wild oscillations but stresses at the grid nodes has a smooth variation and have a physically realistic magnitude. An important observation is that when the deformation gradient is used to display the deformed voxels, the consistent deformation pattern observed in Figure 7 can be seen as a verification that a realistic deformation gradient tensor is calculated. This is related to the nature of the elasto-plastic collapse, which for the collapsing soil column is modelled. In accordance with Andersen and Andersen (8), a relative yield function is defined by

$$f_{rel} = \frac{\frac{1}{2}(\sigma_1 - \sigma_3)}{\frac{1}{2}(\sigma_1 + \sigma_3) - c \cdot \cos(\varphi)} \quad (66)$$

Using this definition,  $f_{rel} = 1$  corresponds to yielding while  $f_{rel} = 0$  corresponds to a hydrostatic stress state. Figure 18 shows the relative yield function in the final configuration of the collapsing soil column problem, using the direct material point stresses and the stresses from Eq (58) to calculate  $f_{rel}$ .

As seen from Figure 18, the relative yield function in the final configuration is between 0.4 in the interior of the collapsed column and close to 1 near the surface when using the mapping of stresses from Eq. (58). When using the direct material point stresses, the relative yield function is fluctuating between zero and unity.

In order to have a better estimation of the deformation for elasto-plastic problems, it is useful to perform an analysis, where the deformation gradient tensor is split into an elastic part and a plastic part defined by

$$\mathbf{F}_p = \mathbf{F}_p^e \mathbf{F}_p^{pl}, \quad (67)$$

Where  $\mathbf{F}_p^e$  and  $\mathbf{F}_p^{pl}$  is the elastic and the plastic part of the deformation gradient tensor associated with material point  $p$ , respectively. This multiplicative decomposition is first suggested by Lee

(28). A review of the applications of the multiplicative decomposition including thermoelasticity, elastoplasticity and biomechanics is given by Lubarda (29).

Whereas the total deformation gradient tensor is a unique function of deformation relative to the reference state, the decomposition of Eq. (67) is not unique. The intermediate configuration defined by Eq. (67) is conceptually introduced by a virtual destressing to the reference stress. Often, the destressed reference state will be a stress-free state. However, for the collapsing column, the reference stress is the dept increasing initial stress-state, while it for the two discs are zero stresses. The intermediate configuration is not uniquely determined, as arbitrary local material rotations can be superposed to intermediate configuration, preserving the reference stress state. An approach to circumvent this is taken along with a suggestion of Lubarda (29) namely by introducing the additional requirement that the elastic unloading takes place without rotation.

In order to implement the composite decomposition into classical incremental plasticity theories such as the Mohr-Coulomb model, the following relationship is employed

$$d\epsilon_p^e = \frac{1}{2} ((d\mathbf{F}_p^e)^T + d\mathbf{F}_p^e) - \mathbf{I}, \quad (68)$$

where  $d\epsilon_p^e$  is the increment of elastic engineering strain associated with material point  $p$ , and  $d\mathbf{F}_p^e$  is the increment of the elastic part of the deformation gradient tensor. According to the requirement that the elastic unloading takes place without rotation, the elastic part of the deformation gradient tensor is symmetric and Eq. (68) can be reformulated as

$$d\mathbf{F}_p^e = d\epsilon_p^e + \mathbf{I}, \quad (69)$$

and  $d\epsilon_p^e$  can be extracted from the return mapping scheme of the constitutive model, where

$$d\epsilon_p = d\epsilon_p^e + d\epsilon_p^{pl} \quad (70)$$

In the MPM computational scheme, the infinitesimal quantities in Eq. (70) is replaced by small, finite quantities that depend of the time step, IE:

$$\Delta\epsilon_p = \Delta\epsilon_p^e + \Delta\epsilon_p^{pl} \quad (71)$$

and

$$\Delta\mathbf{F}_p^e = \Delta\epsilon_p^e + \mathbf{I}, \quad (72)$$

The elastic deformation gradient tensor is updated using

$$\mathbf{F}_p^{e,k+1} = \Delta\mathbf{F}_p^e \mathbf{F}_p^{e,k} \quad (73)$$

and for the plastic part is calculated using Eq. (67) as

$$\mathbf{F}_p^{pl,k+1} = \left( \mathbf{F}_p^{e,k+1} \right)^{-1} \mathbf{F}_p^{k+1} \quad (74)$$

For the collapse of the two discs, the components of the deformation gradient tensors are shown in Figure 19. The elasto-plastic decomposition can also be employed in order to find an estimate of the stresses as part of postprocessing rather than just visualize the stresses at the individual

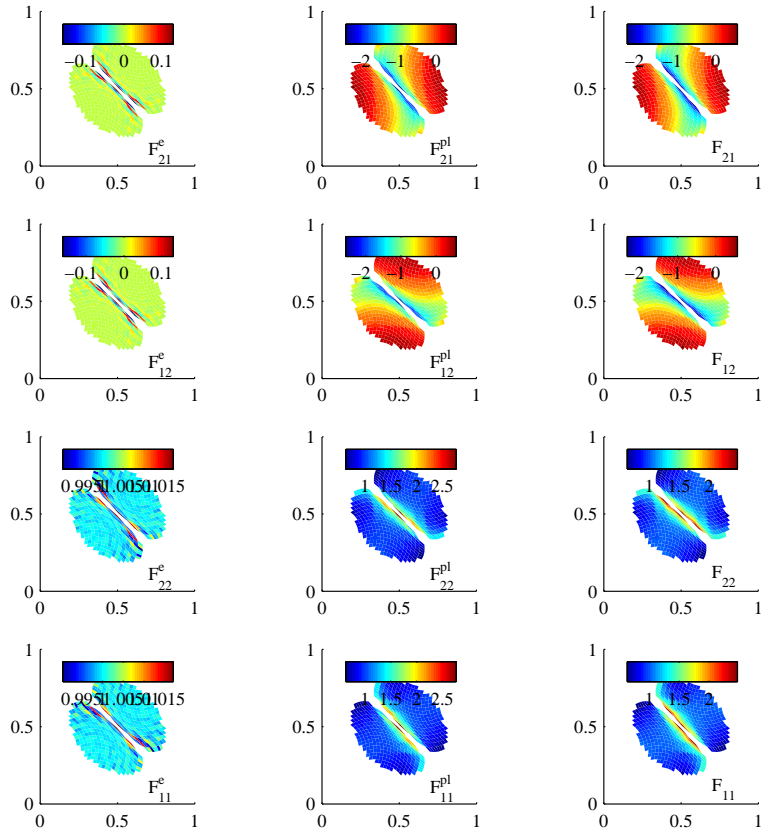


Fig. 19. Multiplicative decomposition of the deformation gradient tensor into an elastic and a plastic part illustrated for the collapse of plastic discs.

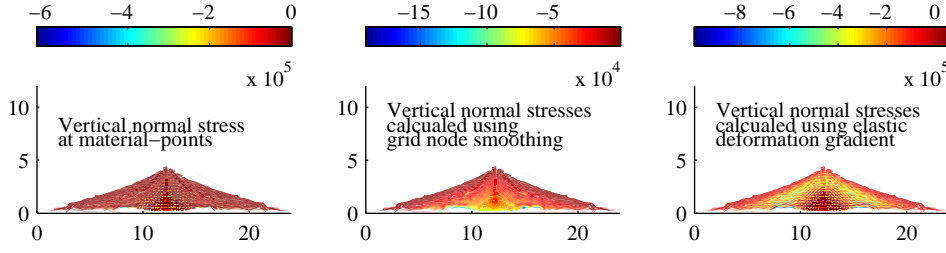


Fig. 20. Vertical normal stresses at the end of the collapse of the soil column, visualized in three different ways.

material points. In that case, first the elastic engineering strain is extracted from the elastic part of the deformation gradient tensor using

$$\boldsymbol{\varepsilon}^e = \mathbf{F}^e - \mathbf{I}, \quad (75)$$

where  $\boldsymbol{\varepsilon}^e$  is the elastic part of the engineering strain tensor relative to the chosen reference (initial) state. Given  $\boldsymbol{\varepsilon}^e$ , the stress change relative to the reference state can then for linear elastic behaviour be calculated as

$$\Delta\boldsymbol{\sigma} = \mathbf{E} : \boldsymbol{\varepsilon}^e, \quad (76)$$

where  $\Delta\boldsymbol{\sigma}$  is stress change, and  $\mathbf{E}$  is the fourth order elasticity tensor. The total stress at the current state is then

$$\boldsymbol{\sigma} = \boldsymbol{\sigma}^{initial} + \Delta\boldsymbol{\sigma} \quad (77)$$

Hence, for elasto-plastic problems, the stresses at the current state can be visualized using post-processing in three different ways; The material-point stresses, the stresses smoothed via the grid nodes, and the stresses calculated using elastic part of the deformation gradient tensor. Figure 20 shows the stresses in the final configuration of the collapsed soil column, using the three visualization techniques. It is observed that the extraction of stresses using Eqs. (75) and (76) improves the visualization of the stress field in this case, but that the most physically plausible stress field is most likely similar to the one calculated using Eq. (58).

## 8 Conclusion

The need to easily verify results visually is of great importance in the application numerical methods. The most established method for numerical modeling is the finite-element method in which a direct visualization of the deformation is obtained. On the contrary, the initial visualizations using the material-point method displayed the physical problem as a collection of points moving around in space in the dynamic simulation. In this article, a new approach to visualizing the deformations is presented for particle based method and exemplified using the material point method. The visualizing technique consists of a three steps. Firstly, a volume is associated with each of the material points. Here, initially rectangular quadrilaterals are chosen to display deformations for two-dimensional problems. The quadrilaterals has the advantage that they are suited for displaying shear unlike if circles were chosen. Secondly, the deformation gradient tensor relatively

to the reference configuration is introduced as a state variable for the particles/points and updated through the dynamic calculation. Finally, the deformation gradient tensor is applied to the initial configuration to calculate a deformed state of each the quadrilateral associated with particle/point and then displayed. It is noted that the applied technique for visualization can also be applied to other particle based methods, for instance to Smoothed Particle Hydrodynamics. Using this type of visualization technique it is possible to get a much better visualization of the deformation. The visualization provides an easy way to evaluate the quality of the results, just such as in the finite element method where it is straightforward to see if a mesh is entangled. Several perspectives of the visualization technique are mentioned. Firstly, in the case of the extreme deformations, it may be possible to introduce a way to split material points into new ones if they become too distorted. The combination of the volume weighted GIMP approach and the tracking of the deformation will provide the framework for splitting. Secondly, the tracking of the deformed configuration makes it possible to increase the accuracy or consistency when dealing with large deformations. It may also be possible to obtain a better evaluation of the GIMP weighting functions when the domains occupied by the material points become distorted.

A particular useful the postprocessing tools presented involves extraction of the physical part of the stresses. It is observed and reported, that stresses at the individual material points often oscillates in a very unphysical fashion but that the deformation pattern in most cases is realistic. A simple postprocessing by mapping the stresses to the grid nodes and back to the material points provides a way to extract a physical part of the stress field, and also suggest why the displacements generally seems correct despite the very oscillatory stresses. It also pinpoints the limitation of the material-point method in its current form.

## References

- [1] D. Sulsky, Z. Chen, H. Schreyer, A particle method for history-dependent materials, *Computer Methods in Applied Mechanics and Engineering* 118 (1994) 179–196.
- [2] D. Sulsky, S. Zhou, H. Schreyer, Application of a particle-in-cell method to solid mechanics, *Computer Physics Communications* 87 (1995) 236–252.
- [3] D. Sulsky, H. Schreyer, Axisymmetric form of the material point method with applications to upsetting and Taylor impact problems, *Computer Methods in Applied Mechanics and Engineering* 139 (1996) 409–429.
- [4] S. Cummins, J. Brackbill, An implicit particle-in-cell method for granular materials, *Journal of Computational Physics* 180 (2002) 506–548.
- [5] I. Babuška, A. Miller, The post-processing approach in the finite-element method - part 2: The calculation of stress intensity factors., *International Journal for Numerical Methods in Engineering* 20 (1984) 1111–1129.
- [6] I. Babuška, A. Miller, The post-processing approach in the finite-element method - part 1: Calculation of displacements, stresses and other higher derivatives of the displacements., *International Journal for Numerical Methods in Engineering* 20 (1984) 1085–1109.
- [7] I. Babuška, A. Miller, The post-processing approach in the finite-element method - part 3: A *posteriori* error estimates and adaptive mesh selection., *International Journal for Numerical Methods in Engineering* 20 (1984) 2311–2324.

- [8] S. Andersen, L. Andersen, Modelling of landslides with the material-point method., *Computers and Structures* 14 (2009) 137–147.
- [9] J. Guilkey, J. Weiss, Implicit time integration for the material point method: Quantitative and algorithmic comparisons with the finite element method, *International Journal for Numerical Methods in Engineering* 57 (2003) 1323–1338.
- [10] S. Andersen, Material-point analysis of large strain problems - modelling of landslides, Ph.D. thesis, Aalborg University (2009).
- [11] A. Choudhury, M. Steffen, J. Guilkey, S. Parker, Enhanced understanding of particle simulations through deformation-based visualization, *Computer Methods in Engineering and Sciences* 63 (2010) 117–136.
- [12] W. Shin, Numerical simulation of landslides and debris flow using an enhanced material point method, Ph.D. thesis, University of Washington (2009).
- [13] S. Andersen, L. Andersen, Analysis of spatial interpolation in the material-point method, *Computers and Structures* 88 (2010) 506–518.
- [14] S. Bardenhagen, E. Kober, The generalized interpolation material point method, *Computer Modelling in Engineering and Sciences* 5 (2004) 477–495.
- [15] J. Ma, L. Hongbing, R. Komanduri, Structured mesh refinement in generalized interpolation material point method (gimp), method for simulation of dynamic problems, *Computer Modelling in Engineering and Sciences* 12 (3) (2006) 213–227.
- [16] M. Steffen, R. Kirby, M. Berzins, Analysis and reduction of quadrature errors in the material point method (MPM), *International Journal for Numerical Methods in Engineering* 76 (2008) 922–948.
- [17] E. Love, D. Sulsky, An unconditionally stable, energy-momentum consistent implementation of the material point method, *Computer Methods in Applied Mechanics and Engineering* 195 (2006) 3903–3925.
- [18] A. York, D. Sulsky, H. Schreyer, The material point method for simulation of thin membranes, *International Journal for Numerical Methods in Engineering* 44 (1999) 1429–1456.
- [19] S. Bardenhagen, J. Brackbill, D. Sulsky, The material-point method for granular materials, *Computer Methods in Applied Mechanics and Engineering* 187 (2000) 529–541.
- [20] S. Bardenhagen, J. Guilkey, K. Roessig, J. Brackbill, W. Witzel, J. Foster, An improved contact algorithm for the material point method and application to stress propagation in granular material, *Computer Modelling in Engineering and Sciences* 2 (2001) 509–522.
- [21] J. Clausen, L. Damkilde, L. Andersen, Efficient return algorithms for associated plasticity with multiple yield planes, *International Journal for Numerical Methods in Engineering* 66 (2006) 1036–1059.
- [22] Z. Wieckowski, S. Youn, J. Yeon, A particle-in-cell solution to the silo discharging problem, *International Journal for Numerical Methods in Engineering* 45 (1999) 1203–1225.
- [23] P. Cleary, J. Monaghan, Conduction modelling using smoothed particle hydrodynamics, *Journal of Computational Physics* 148 (1999) 227–264.
- [24] G. Liu, *Smoothed Particle Hydrodynamics: A meshfree particle method*, World Scientific Publishing Company, 2002.

- [25] J. Monaghan, Smoothed particle hydrodynamics, *Reports on Progress in Physics* 68 (2005) 1703–1759.
- [26] Plaxis bv, Delftechpark 53, 2628 XJ Delft, The Netherlands, PLAXIS - Reference Manual (2010).
- [27] C. Jog, The explicit determination of the lograithm of a tensor and its derivatives, *Journal of Elasticity* 93 (2008) 141–148.
- [28] E. Lee, Elastic-plastic deformation at finite strains, *Journal of Applied Mechanics* 36 (1969) 1–6.
- [29] V. Lubarda, Constitutive theories based on the multiplicative decomposition of deformation gradient: Thermoelasticity, elastoplasticity, and biomechanics, *Applied Mechanics Reviews* 57 (2004) 95–108.

